Spin-Mixing Enhanced Proximity Effect in Aluminum-Based Superconductor–Semiconductor Hybrids

Mazur, Grzegorz P.; van Loo, Nick; Wang, J.; Dvir, Tom; Wang, Guanzhong; Korneychuk, S.; Borsoi, Francesco; Dekker, Robin C.; Badawy, Ghada; Vinke, Peter

DOI
10.1002/adma.202202034

Publication date
2022

Document Version
Final published version

Published in
Advanced Materials

ADVANCED MATERIALS
www.advmat.de

Spin-Mixing Enhanced Proximity Effect in Aluminum-Based Superconductor–Semiconductor Hybrids

Grzegorz P. Mazur, Nick van Loo, Ji-Yin Wang, Tom Dvir, Guanzhong Wang, Aleksei Khindanov, Svetlana Korneychuk, Francesco Borsoi, Robin C. Dekker, Ghada Badawy, Peter Vinke, Sasa Gazibegovic, Erik P. A. M. Bakkers, Marina Quintero-Pérez, Sebastian Heedt, and Leo P. Kouwenhoven*

In superconducting quantum circuits, aluminum is one of the most widely used materials. It is currently also the superconductor of choice for the development of topological qubits. However, aluminum-based devices suffer from poor magnetic field compatibility. Herein, this limitation is resolved by showing that adatoms of heavy elements (e.g., platinum) increase the critical field of thin aluminum films by more than a factor of two. Using tunnel junctions, it is shown that the increased field resilience originates from spin-orbit scattering introduced by Pt. This property is exploited in the context of the superconducting proximity effect in semiconductor–superconductor hybrids, where it is shown that InSb nanowires strongly coupled to Al/Pt films can maintain superconductivity up to 7 T. The two-electron charging effect is shown to be robust against the presence of heavy adatoms. Additionally, non-local spectroscopy is used in a three-terminal geometry to probe the bulk of hybrid devices, showing that it remains free of sub-gap states. Finally, it is demonstrated that proximitized semiconductor states maintain their ability to Zeeman-split in an applied magnetic field. Combined with the chemical stability and well-known fabrication routes of aluminum, Al/Pt emerges as the natural successor to Al-based systems and is a compelling alternative to other superconductors, whenever high-field resilience is required.

1. Introduction

Topological superconductivity can arise in hybrid material stacks containing a conventional superconductor and a semiconductor with strong Rashba spin-orbit coupling.[1,2] Narrow-gap semiconductors with a large g-factor and low carrier density (such as InAs and InSb) are most commonly used, either as 1D nanowires[3] or 2D electron gases.[4] The first generation of semiconductor–superconductor hybrids was made using Nb[5] and NbTiN[6] as the superconductor. While these materials offer a large superconducting gap and resilience to high magnetic fields, the hybrids suffered from a finite in-gap conductance (often described as "soft-gap"). In addition, Nb-based hybrids have not been shown to host parity-conserving transport—a key ingredient for the development of topological qubits.[7] These drawbacks remained even after substantial improvements of the fabrication, such as epitaxial growth of the superconductor.[8]

In the meantime, aluminum has emerged as the material of choice. Thin shells made of this metal combined with an oxide-free interface result in clean electronic transport.[9,10] This includes suppressed sub-gap tunneling conductance (hard induced gap) and parity-conserving transport,[11] which enables the search for topological superconductivity. For a topological phase to emerge, the minimal condition states that the Zeeman energy $V_Z = g\mu_B B$ must be larger than the induced

G. P. Mazur, N. van Loo, J.-Y. Wang, T. Dvir, G. Wang, S. Korneychuk, F. Borsoi, R. C. Dekker, P. Vinke, M. Quintero-Pérez, S. Heedt, L. P. Kouwenhoven
QuTech and Kavli Institute of Nanoscience
Delft University of Technology
Delft 2600 GA, The Netherlands
E-mail: g.p.mazur@tudelft.nl

The ORCID identification number(s) for the author(s) of this article can be found under https://doi.org/10.1002/adma.202202034.

DOI: 10.1002/adma.202202034

A. Khindanov
Department of Physics
University of California
Santa Barbara, CA 93106, USA

G. Badawy, S. Gazibegovic, E. P. A. M. Bakkers
Department of Applied Physics
Eindhoven University of Technology
Eindhoven 5600 MB, The Netherlands

M. Quintero-Pérez
Netherlands Organisation for Applied Scientific Research (TNO)
Delft 2600 AD, The Netherlands

superconducting gap Δ, where g is the Landé g-factor, μ_B is the Bohr magneton, and B is the applied magnetic field. It was demonstrated recently that the properties of the semiconductor, such as spin-orbit coupling and g-factor, are renormalized by the presence of a proximitizing metal.[12,13] As a result, stronger magnetic fields than initially anticipated are required to close and reopen the induced superconducting gap.[14] Typical aluminum-based hybrids, however, have a zero-field superconducting gap Δ_0 ranging from 200 to 300 μeV,[6] which results in poor field compatibility.

This has fueled the search for alternative superconducting systems, with recent works reporting superconductivity and parity-conserving transport in InSb/Sn,[15] InAs/Pb,[16,17] and InAs/In[18] hybrids. These superconductors offer higher field compatibility than aluminum, yet they bring different challenges such as chemical instability and fabrication constraints.[19,20] To avoid these constraints, in this work we present a different approach by eliminating the main drawback of aluminum: its poor resilience against magnetic fields.

For a Bardeen–Cooper–Schrieffer (BCS) type superconductor like aluminum, there are two dominant mechanisms which quench superconductivity in a finite magnetic field. The first of these is orbital depairing, which results from the cyclotron motion of conduction electrons due to the magnetic field.

If the superconductor is grown as a thin film, this mechanism can be suppressed when the field is applied in the plane of the film. For light elements such as Al, there is a second contribution arising from spin physics. Once the magnetic field reaches a certain value, the paramagnetic ground state becomes energetically favorable. This results in a first-order phase transition into the normal state. The field for which this happens is known as the Chandrasekhar– Clogston[21,22] or Pauli limit, and is given by $B_P = \Delta_0/(\sqrt{2}\mu_B)$. In addition, the quasiparticle excitation spectrum spin-splits upon applying a magnetic field. In their seminal experiment,[23] Tedrow and Meservey demonstrate that Zeeman splitting can be quenched and eventually suppressed completely through the addition of heavy metal impurities, such as platinum (Pt). These heavy atoms introduce spin-orbit scattering, which prevents spins from being polarized by an external magnetic field. As a result, superconductors made of lightweight elements can reach unprecedentedly high critical fields. This has straightforward applications in the field of semiconductor–superconductor hybrids, where large Zeeman energies are a necessary condition for achieving a topological superconducting phase.

2. Al/Pt Thin Films and Tunnel Junctions

We begin this study by evaluating the properties of aluminum films with a thickness of 6 nm, coated with varying amounts of platinum. We define the platinum thickness d_{Pt} as measured by the quartz balance in the deposition chamber (for details of the calibration see Section S1.1, Supporting Information[24]). **Figure 1** presents the superconducting transitions of Al/Pt films as a function of temperature (Figure 1a) and in-plane magnetic field (Figure 1b).

Importantly, the addition of Pt does not affect the shape and sharpness of the superconducting transitions, which indicates that the films do not become strongly disordered or inhomogeneous.[25] The bare aluminum film has a critical temperature T_c = 1.79 K and in-plane critical field B_c = 2.6 T. Upon the addition of platinum, the critical field is increased above the bare aluminum's Chandrasekhar– Clogston limit already for $d_{Pt} \approx 1$ Å, while leaving T_c unaffected. In agreement with previous studies on Al/Pt bilayers,[23] the critical field starts to saturate for $d_{Pt} \approx 2$ Å and increases only by an additional 300 mT for $d_{Pt} \approx 5.1$ Å (see Figure 1c). At these thicknesses, however, T_c starts to decrease as a result of the inverse proximity effect, as shown for Au/Be bilayers.[26] Our theoretical model based on the Usadel equation (see Section S1.3, Supporting Information[24]) captures the increase of B_c as a direct result of including spin-orbit scattering (Figure 1c). The calculated spin-orbit scattering energies increase linearly with d_{Pt},[24] in agreement with previous experiments.[23] In addition, we perform a structural analysis of the films. Figure 1d presents the cross-section of an Al/Pt film with $d_{Pt} \approx 1.9$ Å, which reveals the poly-crystalline structure of the Al. The results of electron energy loss spectroscopy (EELS)[24] performed on the studied samples indicate that aluminum and platinum do not form an alloy, in agreement with the bulk phase diagram.[27]

Furthermore, we investigate the impact of Pt atoms on the Al quasiparticle density of states through normal-metal/insulator/superconductor (NIS) tunneling measurements. A schematic illustration together with the used measurement circuit for these experiments is shown in **Figure 2**c. Further details on the fabrication and measurements can be found in Section S1.2, Supporting Information.[24] For the aluminum film, we observe a Zeeman splitting of the quasiparticle coherence peaks (Figure 2a). At an in-plane magnetic field of $B_{\parallel}$ = 3.45 T, the film undergoes a first-order phase transition to the normal state. Our theoretical model reproduces these two key features (Figure 2d), where the first-order transition is reflected in an abrupt collapse of the order parameter.

The critical field extracted from the model is 200 mT smaller than the experimentally measured value. This discrepancy between theory and experiment can be explained by the hysteretic behavior of the order parameter near the transition[28] (see Figure S3, Supporting Information[24]). A metastable superconducting state can persist for magnetic fields slightly above the calculated critical value.

For the Al/Pt film with d_{Pt} = 1.9 Å, Zeeman splitting is not observed. Instead, the film undergoes a second-order phase transition at $B_{\parallel}$ = 6.34 T induced primarily by orbital effects (Figure 2b). Importantly, the energy gap in the film remains free of quasiparticle states (for log-scale linecuts, see Figure S4, Supporting Information[24]). Theoretical modeling of the film reveals a small magnetic field range with gapless superconductivity close to the transition (Figure 2e), which is an expected feature when the transition from the superconducting into the normal state is of second order.[29] For both Al and Al/Pt films, the model yields diffusion constants which correspond to a mean free path of $l_{mfp} \approx 7$ Å. This value is consistent with reports on Al films grown under similar conditions.[30,31] Since the addition of Pt does not seem to affect the mean free path, the increase in critical magnetic field cannot be attributed to increased disorder. The suppression of Zeeman splitting instead demonstrates that spin mixing

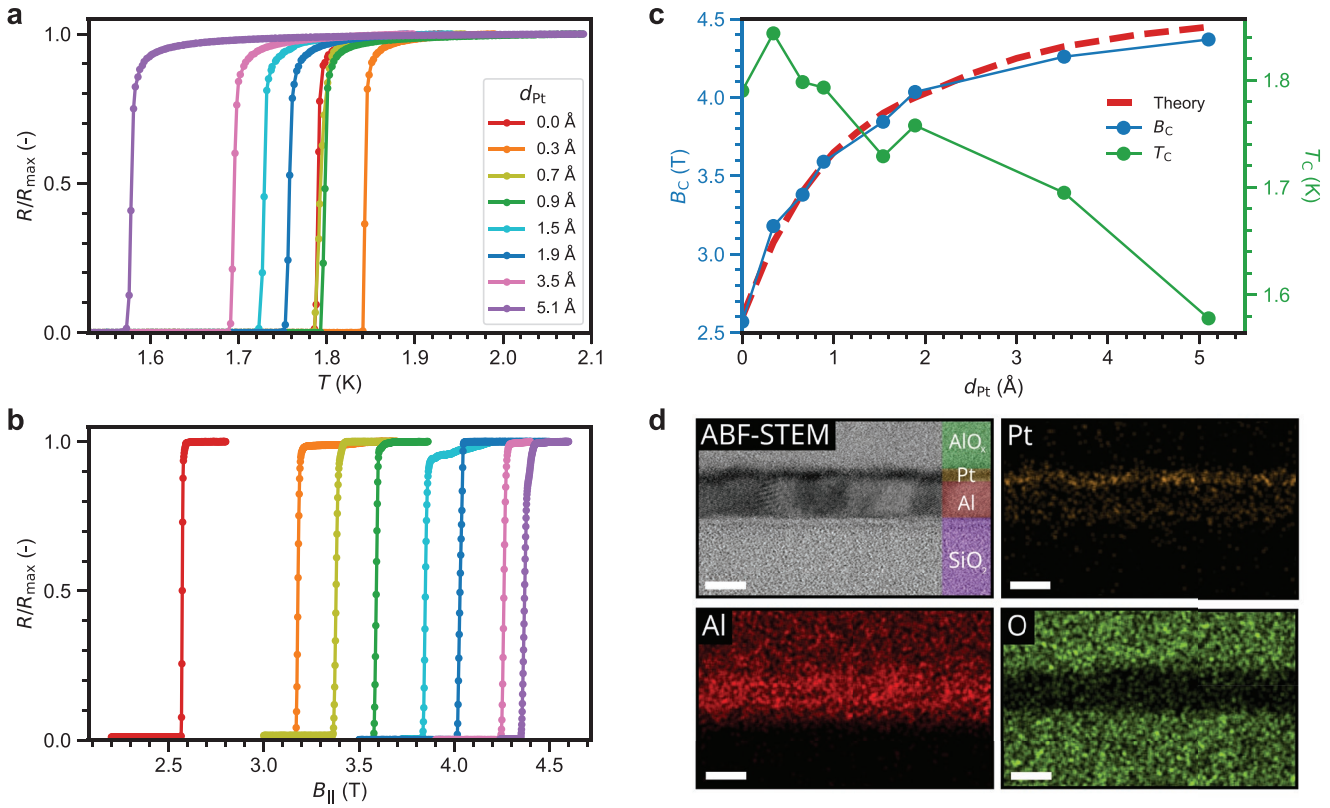

Figure 1. Properties of Al/Pt thin films. Four-point measurements of resistance R normalized to its value in the normal state R_N as a function of a) temperature and b) in-plane magnetic field. Measurements have been performed for 6 nm thick aluminum films with varying amount of platinum d_{Pt}. c) In-plane critical magnetic field and temperature as a function of Pt thickness, together with the predicted critical field from theory calculations. d) Annular bright field scanning-tunneling electron micrograph and energy-dispersive X-ray images of the Al film with 1.89 Å of Pt. The thin layer of platinum (orange) is visible on top of aluminum film (red). The film is grown on top of amorphous SiO_2 and amorphous AlO_x on top of the film serves as the capping layer. Scale bars are 5 nm.

is the dominant mechanism. From the model, the increased spin-orbit scattering energy of the Al/Pt film is extracted to be $\Gamma_{SO} = 7.5$ meV, corresponding to a spin-orbit scattering time of $\tau_{SO} = 1.3 \times 10^{-13}$ s. We note, however, that this extracted value of the spin-orbit scattering energy could be overestimated due to the presence of Fermi-liquid effects[32] (see discussion in Section S1.4, Supporting Information[24]). In Figure 2f, the measured energy gap is shown together with the energy gap extracted from theory, as well as the corresponding order parameter. We observe good quantitative agreement between the model and our experiment.

3. Spectroscopy and Coulomb Blockade of InSb/Al/Pt Hybrids

The next step of our study is to induce superconductivity in InSb nanowires using Al/Pt films. In order for any material combination to be considered for Majorana experiments and topological qubits, two fundamental properties need to be demonstrated.

In tunneling spectroscopy, a proximity-induced gap free of sub-gap states (i.e., a hard gap) should be observed. While this is conventionally done on hybrids with a grounded superconductor, designs of topological qubits typically contain superconducting segments which are floating.[7] These have a finite charging energy, and it is energetically favorable to add charges to such an island in pairs if the low-energy excitation spectrum of the hybrid is free of single-charge states (i.e., $2e$ charging). Both a hard superconducting gap and $2e$ charging have already been demonstrated for Al-based hybrids.[3,11,33] In order to confirm that platinum does not compromise these properties, for example through hosting single-electron states,[34] hybrids with a grounded superconducting shell as well as with a floating shell have been investigated.

In **Figure 3**, we show the results of both tunneling spectroscopy and Coulomb blockade measurements on InSb/Al/Pt nanowires. The fabrication follows our shadow-wall lithography method,[9,10] of which details can be found in Sections S1.5, S1.6, and S1.7, Supporting Information.[24] In Figure 3a, schematic illustrations and measurement circuits of a tunneling spectroscopy device (top) and a superconducting island device (bottom) are shown. SEM images of all the measured devices are shown in Figure S7, Supporting Information.[24] The measurements are conducted by applying a bias voltage between the source and drain contacts. The chemical potential in the hybrid is controlled by the so-called super gate voltage V_{SG}, while the tunnel gate voltages V_{TG} are used to induce tunnel barriers in

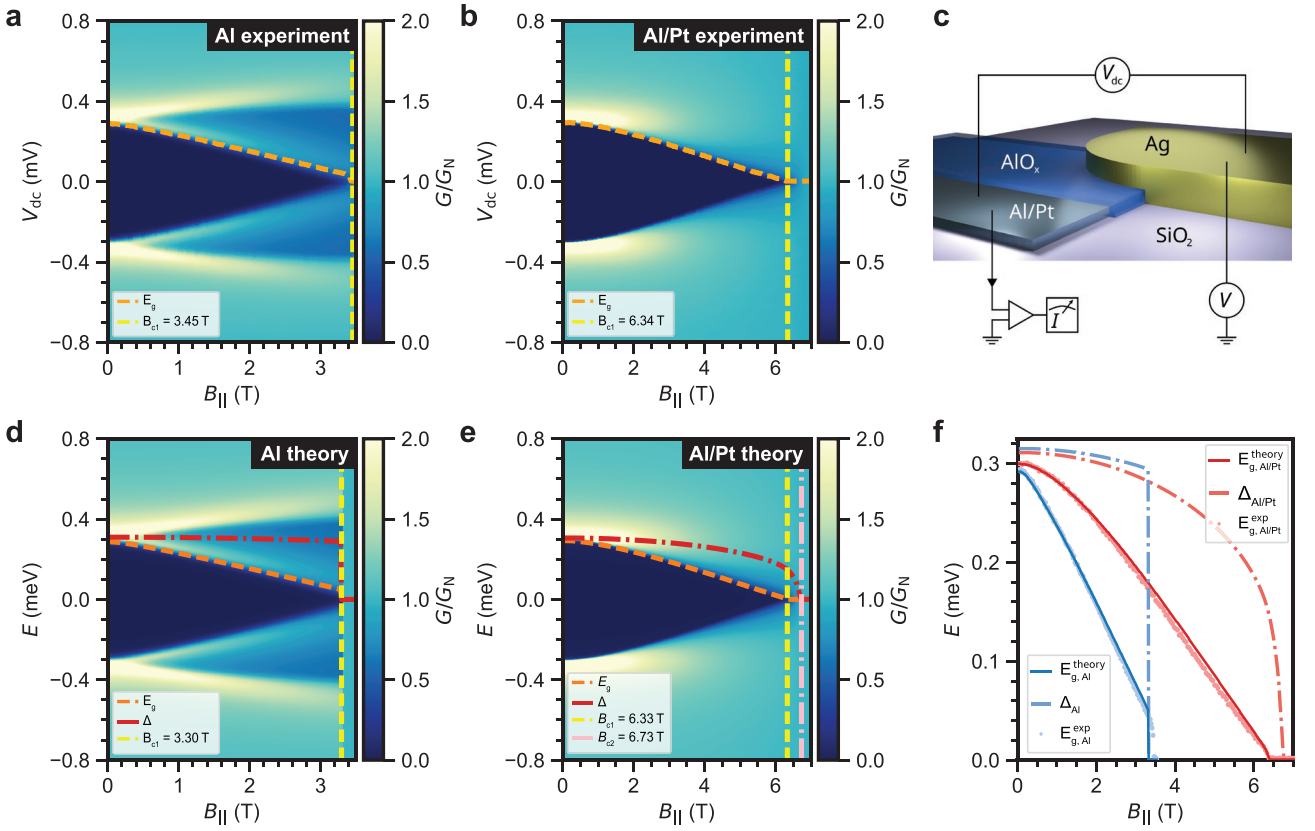

Figure 2. Conductance spectroscopy on Al and Al/Pt NIS tunnel junctions. a) Experimental tunneling conductance of a ≈4.5 nm Al tunnel junction. b) Experimental tunneling conductance of a ≈4.5 nm Al + 1.9 Å Pt tunnel junction. c) Schematic and measurement circuit of a NIS tunnel junction. The tunnel barrier is formed by the AlO_x layer between the Al/Pt and Ag electrodes. d) Tunneling conductance from theory calculations of the Al tunnel junction. e) Tunneling conductance from theory calculations of the Al/Pt tunnel junction. The dashed orange lines present the energy gap E_g. The order parameter Δ which is extracted from theory is presented by dashed red lines. Dashed yellow lines show the magnetic field B_{c1} for which the energy gap is closed, and the dashed pink lines indicate the magnetic field B_{c2} for which the order parameter is calculated to vanish. f) Overview of the extracted energy gap from experiments, the predicted energy gap from theory and the corresponding order parameter of the films.

the nanowire junctions. Details of the measurements can be found in Section S1.8, Supporting Information.

In order to measure the spectroscopy device, the semiconducting nanowire junction is tuned into the tunneling regime. Under this condition, the measured differential conductance reflects the quasiparticle density of states (DOS) in the proximitized section of the nanowire. Here, the super gate voltage is set to $V_{SG} = -1$ V, where a strong coupling between the nanowire and the superconducting shell is expected.[13,35] The differential conductance is shown as a function of magnetic field parallel to the nanowire axis in Figure 3d, with linecuts taken at $B = 0.0$ T and $B = 4.5$ T presented in Figure 3e. At zero magnetic field, a large superconducting gap of $\Delta = 304$ μeV is observed. This is significantly larger than in the case of conventional Al-based hybrids, which is a direct consequence of the reduced thickness (≈4.5 nm) of the Al shell.[23]

In addition, the in-gap conductance is suppressed by two orders of magnitude and the differential conductance matches the BTK theory,[36] indicating that the superconducting gap is free of sub-gap states (i.e., a hard gap). Importantly, at B = 4.5 T the superconducting gap is still on the order of ≈100 μeV, which allows to look for Majorana signatures at Zeeman energies which were not accessible before. Remarkably, as can be seen from the in-gap and out-of-gap linecuts in Figure 3f, the superconducting gap remains hard up to $B = 6.0$ T. The field compatibility offered by Al/Pt hybrids opens up the opportunity to study high-field signatures of Majorana zero modes, like Majorana oscillations.[37] The superconducting island device is studied by inducing tunnel barriers in the semiconducting nanowire junctions, which separate the island from the leads. The voltage on the super gate is then swept to tune the charge on the island, as shown in Figure 3b. This results in a periodic sequence of 2*e* Coulomb diamonds with a charging energy $E_c \approx 30$ μeV. Linecuts are shown in Figure 3c, where at finite bias the Coulomb peak periodicity has doubled due to the onset of single-electron transport in the quasiparticle excitation spectrum. The magnetic field evolution is shown in Figure S12, Supporting Information.[24] The observation of 2*e* charging demonstrates that semiconductors coupled to Al/Pt are a suitable replacement of Al-based hybrids, capable to be used for the development of parity-protected topological qubits. Additional data on tunneling spectroscopy devices and superconducting islands is shown in Section S2, Supporting Information.

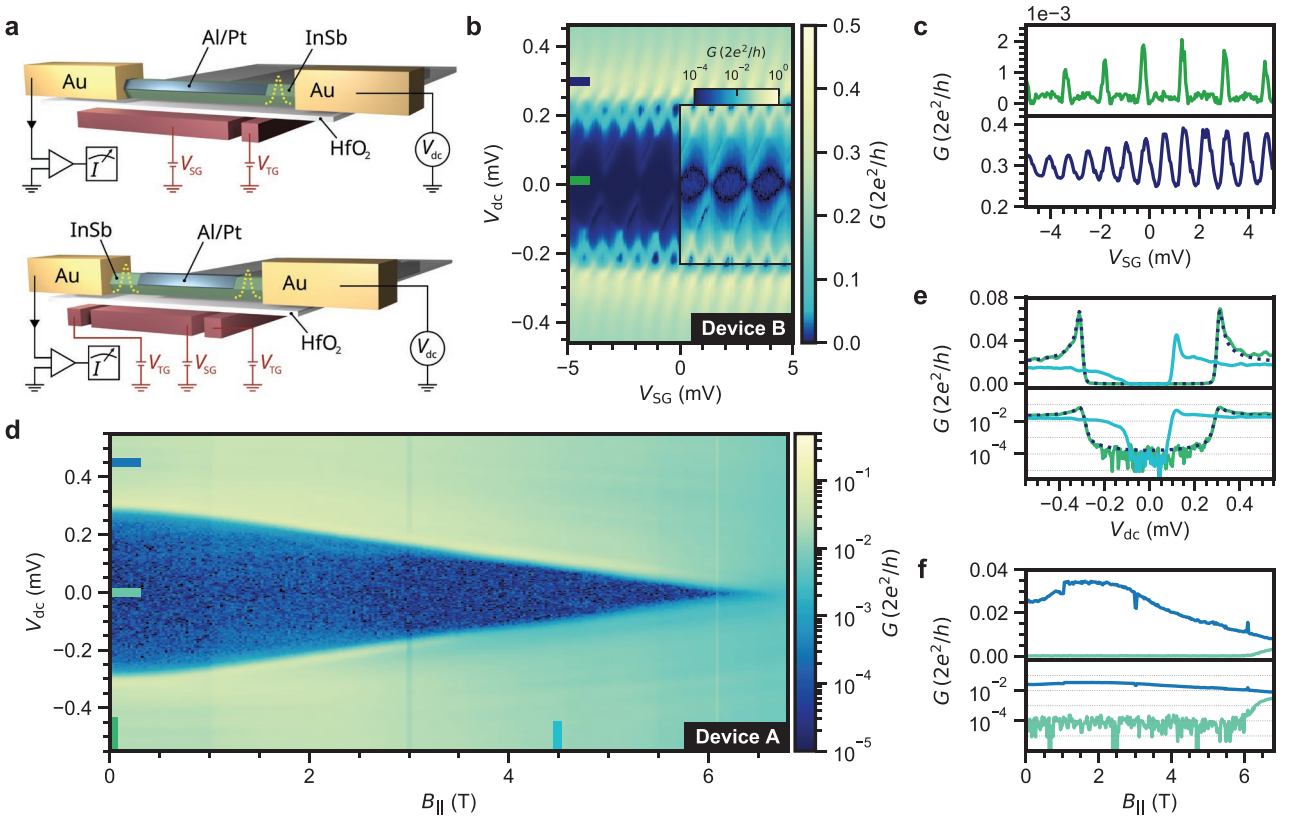

Figure 3. Transport data on 2-terminal InSb/Al/Pt hybrids (devices A and B). a) Schematics of devices used for tunneling spectroscopy (top, device A) and Coulomb blockade spectroscopy (bottom, device B). Device A has a grounded superconducting shell of 1.8 µm long, while the floating shell of Device B is 0.8 µm long. Dashed yellow potentials indicate the formation of tunnel barriers in the semiconducting junctions. b) 2*e*-periodic Coulomb diamonds measured on device B. The inset is a logarithmic overlay of the Coulomb diamonds, highlighting the 2*e* periodicity at low biases. c) Linecuts from the Coulomb-blockade measurements in panel (b) at the locations designated by the colored lines. d) Differential conductance from tunneling spectroscopy of device A in logarithmic scale, taken at $V_{SG} = -1$ V as a function of parallel magnetic field. e) Linecuts from the tunneling spectroscopy measurement in panel (d) at the locations designated by the colored lines, shown in linear (top) and logarithmic (bottom) scale. The dashed lines show conductance from BTK theory, with $\Delta = 304$ µeV, temperature $T = 70$ mK and transmission $G_N = 0.018\ G_0$. f) Differential conductance taken from the tunneling spectroscopy measurement in panel (d) at the locations designated by the colored lines, shown in linear (top) and logarithmic (bottom) scale.

4. Non-Local Measurements of Three-Terminal Hybrids

The experiments presented above are a prerequisite for investigating topological superconductivity. Most of the research to date has focused on the study of zero-bias anomalies and their evolution as a function of chemical potential and magnetic field.[6,38] However, it is becoming increasingly clear that spectroscopy of the density of states at the ends of a nanowire is inconclusive when it comes to identifying an extended topological superconducting phase.[39,40] While conventional tunneling experiments can provide information on the local density of states at both ends of a wire, the induced gap in the bulk of the hybrid can instead be probed by measuring the non-local conductance in a three-terminal geometry.[41] Consequently, the observation of correlated zero-bias peaks at both ends of a wire should be accompanied by the closing and reopening of the induced superconducting gap in the non-local spectra.[42]

In **Figure 4**a we present a schematic of such a three-terminal device, together with the measurement circuit. The Al/Pt shell covers three facets of the InSb nanowire and is directly connected to the film on the substrate. This forms the third lead of the device, which we connect to ground in the presented measurements. The super gate voltage V_{SG} controls the chemical potential in the hybrid, and the tunnel gate voltages, V_{TL} and V_{TR}, are used to control the left and right semiconducting nanowire junction conductances, respectively. In this work, we fix the super gate voltage to be $V_{SG} = -2$ V, where the nanowire is expected to be strongly coupled to the superconducting shell.[13,35] Bias voltages are applied to the left (V_L) or right (V_R) normal contact while keeping the middle lead grounded. The local (g_{LL}, g_{RR}) and non-local (g_{LR}, g_{RL}) conductances are measured to form the full conductance matrix of the system, where they are defined as $g_{ij} \equiv dI_i/dV_j$. Figure 4c–f shows an example of such a conductance matrix, measured as a function of parallel magnetic field.

The critical field in this device is reduced to ≈4 T in comparison to the single-facet device in the previous section. This is a direct consequence of the thicker Al/Pt shell (≈8 nm), in which the orbital depairing is more pronounced. The local spectrum on the right junction exhibits a few sub-gap states, which are not present in the local spectrum on the left junction. This suggests that these states are confined locally near the right junction. The corresponding non-local conductances

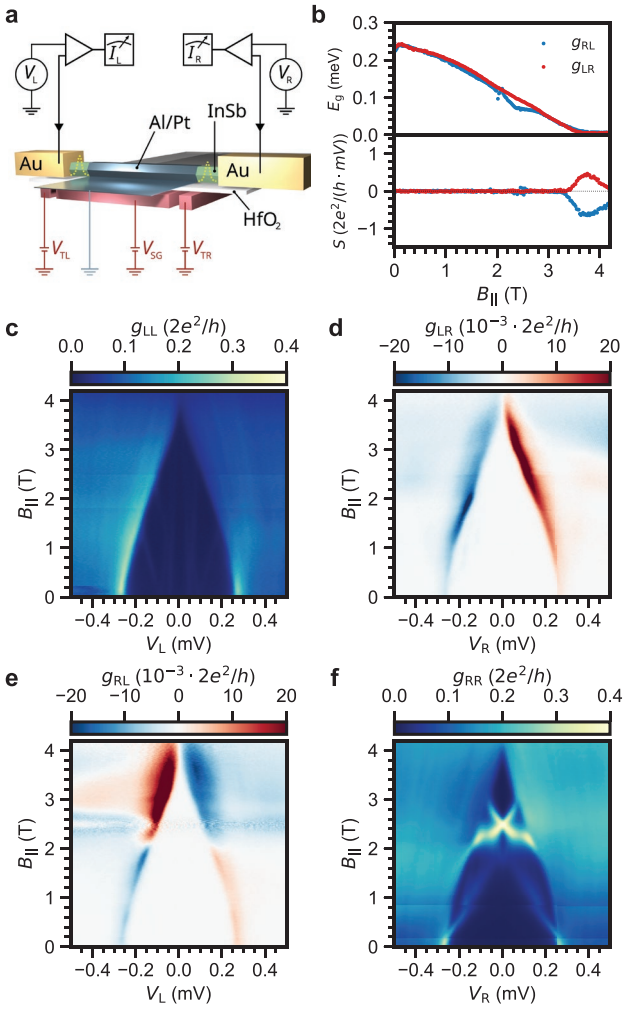

Figure 4. Three-terminal measurements on InSb/Al/Pt hybrids (device C). a) Schematic of a three-terminal hybrid device and the measurement circuit. The hybrid has a superconducting shell of 1 µm in length, which is grounded through its connection to the film on the substrate. Yellow dashed potentials indicate the formation of tunnel barriers in the semiconducting junctions. b) Extracted energy gap in the bulk of the hybrid (top), together with the non-local slope at zero bias (bottom). c–f) Differential-conductance matrix measurements as a function of parallel magnetic field. Panels (c,f) show the local conductances g_{LL} and g_{RR}, respectively, whereas panels (d,e) present the non-local conductances g_{LR} and g_{RL}. Conductances are defined as $g_{ij} \equiv dI_i/dV_j$. Data is taken at $V_{SG} = -2$ V.

are zero everywhere inside the gap, confirming the local nature of these sub-gap states. This is emphasized in Figure 4b, which displays the extracted energy gap E_g in the hybrid (top panel) as well as the non-local slope $S \equiv d^2I_i/dV_j^2|_{V_j=0}$ (bottom panel). The non-local slope stays close to zero only while there is an energy gap present in the bulk of the hybrid. It starts to deviate from zero around $B_\parallel \approx 3.4$ T, indicating the gap in the system becomes soft before closing eventually around $B_\parallel \approx 3.8$ T. Remarkably, the induced superconducting gap in the bulk of these hybrids can be free of sub-gap states up to high magnetic fields. The effect of the super gate voltage on the proximity effect in these hybrids will be explored in an upcoming work. The extraction procedure for the energy gap and the non-local slope is described in Section S1.8, Supporting Information.

5. Zeeman Splitting Inside the Hybrid

Having shown that the addition of Pt adatoms quenches the Zeeman effect in the Al shell, we turn our attention to the semiconductor part of the hybrid device. Breaking the Kramers degeneracy through Zeeman splitting of the DOS of the hybrid segment lies at the heart of the proposed schemes to reach the topological regime.[1,2] Tunneling into a discrete Andreev bound state (ABS) in the hybrid nanowire involves a transition between a spinless singlet state and spinful doublet states. The doublet state splits under the effect of an external magnetic field.[43,44] Thus, measuring the evolution of the ABS spectrum in a magnetic field would show whether the effect of spin mixing leaks to the proximitized semiconductor.

Figure 5a shows a schematic illustration and the measurement circuit of another three-terminal device, with a hybrid segment 150 nm long. The local conductance g_{LL} as a function of V_{SG} and V_L taken at zero field is shown in Figure 5b.

We observe a clean superconducting gap, in addition to a series of sub-gap resonances. They appear only when setting $V_{SG} > 0$ V, and reflect the presence of discrete states in the confined semiconductor. These states hybridize with the superconductor to form ABSs. In Figure 5c–f, we track the evolution of the ABSs in an applied magnetic field by measuring the conductance matrix. We set $V_{SG} = 0$ V, so that the energy of one of the ABSs is reduced below the quasiparticle continuum. To verify that the ABS is located in the hybrid segment and is not a local resonance on the left junction, we notice that it appears at the same energy on both sides, in g_{LL} and g_{RR}. We also note that it shows up in the non-local signals, g_{RL} and g_{RL}, consistent with a state which is extended along the entire hybrid. Upon application of the magnetic field, the ABS splits into two peaks that move with the same slope in opposite directions. The outgoing peaks are soon merged with the quasiparticle continuum, but the peaks shifting to lower energy cross at $B = 0.34$ T, where the ABS ground state turns from even to odd.[43] We extract its gyromagnetic ratio to be $g = 20.0 \pm 0.3$, showing only a moderate amount of renormalization of the semiconducting properties.[12,13] Thus, the effect of spin mixing from Pt enhances the critical field of the Al shell, but does not negatively influence the spin properties in the semiconductor. This is evidenced by the picture of an extended ABS in the hybrid segment, which Zeeman splits with a high g factor in the presence of a magnetic field. This demonstration is of crucial importance, as a spin-mixed hybrid would be fundamentally incapable of transitioning into a topological phase. It is still an open question if hybrids would preserve these properties when the semiconductors are coupled to high-atomic-number superconductors, like Sn, In, or Pb.[15,17,18]

6. Conclusion

In this work, we have examined the properties of thin aluminum films coated with sub-monolayer amounts of platinum,

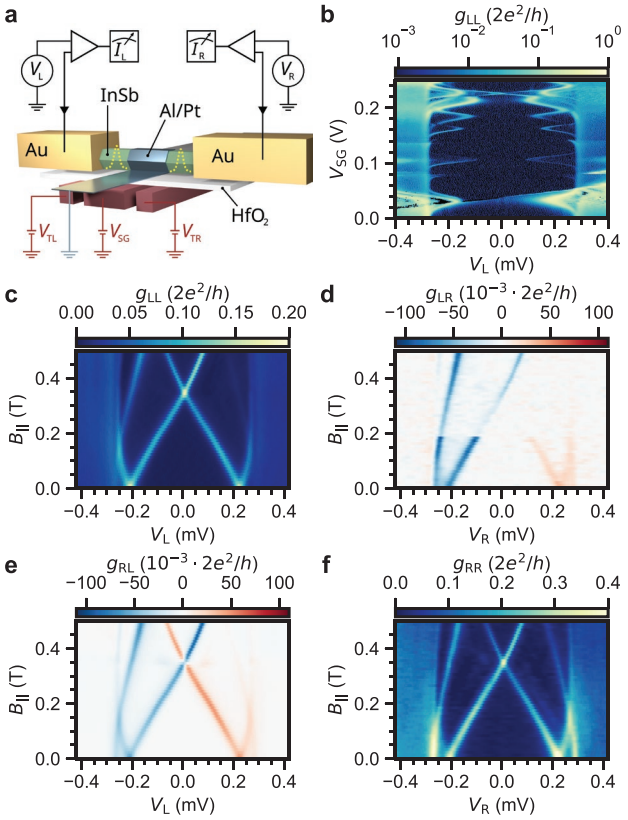

Figure 5. Spin splitting of Andreev bound states in InSb/Al/Pt hybrids (device D). a) Schematic of a three-terminal hybrid and the measurement circuit. The hybrid has a superconducting shell of 150 nm in length, which is grounded through its connection to the film on the substrate. Yellow dashed potentials indicate the formation of tunnel barriers in the semiconducting junctions. b) Local differential conductance as a function of super gate voltage taken at zero applied magnetic field. c–f) Differential-conductance matrix measurements as a function of parallel magnetic field. Panels (c,f) show the local conductances g_{LL} and g_{RR}, respectively, whereas panels (d,e) illustrate the non-local conductances g_{LR} and g_{RL}. Data is taken at $V_{SG} = 0.0$ ~V.

as well as semiconductor nanowires proximitized by Al/Pt bilayers.

By measuring the critical temperature and parallel magnetic field of thin films, we have found that ≈2 Å of Pt can increase the critical field above the Chandrasekhar– Clogston limit without having a significant effect on the size of the superconducting gap. We show, using our theoretical model, that the spin-orbit scattering rate of Pt-covered films is drastically increased. At the same time, various critical parameters of the films, such as the mean free path and coherence length, remain unaffected. When coupling InSb nanowires to these Pt-enhanced films, we observe a hard superconducting gap up to magnetic fields as high as 6 T. Additionally, parity-conserving transport results in the formation of 2*e*-periodic diamonds in Coulomb-blockade experiments. Upon switching to a three-terminal geometry, non-local measurements provide evidence of a bulk energy gap which is free of sub-gap states. Furthermore, the spin splitting of extended ABSs in a short hybrid is observed. This evidences that the spin mixing from Pt does not adversely affect the semiconducting properties of a hybrid. Crucially, like Al, the Al/Pt system satisfies all the necessary requirements for investigating Majorana zero modes and topological qubits.

What should also be considered is that the fabrication of aluminum/platinum samples can be straightforwardly executed, with minimal modifications of the well-established aluminum technology. Importantly, aluminum and platinum are non-toxic materials suited for most UHV deposition chambers. As a result, the development of scalable quantum systems can be readily implemented using Al/Pt bilayers—which is still a major challenge for heavy elements with a low melting point like Sn and Pb. Thus, we expect that Al covered with Pt will be the natural successor to Al-based hybrids. Furthermore, since Al can be grown especially thin in planar geometries, we anticipate that Al/Pt will be particularly attractive for proximitizing 2D semiconductors and van der Waals materials. Future works involving Al/Pt hybrids will focus on investigating Majorana physics, exploring their behavior as a function of chemical potential and high Zeeman energies.

Supporting Information

Supporting Information is available from the Wiley Online Library or from the author.

Acknowledgements

The authors thank Andrey Antipov, Philippe Caroff, William Cole, Dmitry Pikulin, Anton Akhmerov and Roman Lutchyn for helpful discussions. The authors also thank Jan Cornelis Wolff, Mark Ammerlaan, Olaf Benningshof, and Jason Mensingh for valuable technical support. The authors are grateful to Kongyi Li and Mariusz Andrzejczuk for the help with the TEM lamella preparation. This work was financially supported by the Dutch Organization for Scientific Research (NWO), the Foundation for Fundamental Research on Matter (FOM) and Microsoft Corporation Station Q.

Conflict of Interest

The authors declare no conflict of interest.

Author Contributions

G.P.M. and N.v.L. contributed equally to this work. G.P.M. and N.v.L. conceived the experiment. G.P.M. and N.v.L. fabricated and measured the devices. T.D. and G.W. performed the measurements and analysis of device D. J.Y.W., R.C.D., F.B., P.V., and S.H. assisted with sample fabrication and/or measurements. G.P.M. and N.v.L. analyzed the transport data. A.K. provided theoretical modelling and analysis of the film and tunnel junction data. S.K. performed the TEM analysis. G.B., S.G. and E.P.A.M.B. carried out the nanowire synthesis. G.P.M. and N.v.L. wrote the manuscript with valuable input from all authors. L.P.K. supervised the project.

Data Availability Statement

The data is available on Zenodo repositotry with https://doi.org/10.5281/zenodo.5835794.

Keywords

aluminum, high-magnetic-field, nanowires, superconductivity

Received: March 3, 2022
Revised: April 25, 2022
Published online:

[1] R. M. Lutchyn, J. D. Sau, S. Das Sarma, *Phys. Rev. Lett.* **2010**, *105*, 077001.
[2] Y. Oreg, G. Refael, F. Von Oppen, *Phys. Rev. Lett.* **2010**, *105*, 177002.
[3] P. Krogstrup, N. Ziino, W. Chang, S. Albrecht, M. Madsen, E. Johnson, J. Nygård, C. M. Marcus, T. Jespersen, *Nat. Mater.* **2015**, *14*, 400.
[4] J. Shabani, M. Kjaergaard, H. J. Suominen, Y. Kim, F. Nichele, K. Pakrouski, T. Stankevic, R. M. Lutchyn, P. Krogstrup, R. Feidenhans'l, S. Kraemer, C. Nayak, M. Troyer, C. M. Marcus, C. J. Palmstrøm, *Phys. Rev. B* **2016**, *93*, 155402.
[5] M. Deng, C. Yu, G. Huang, M. Larsson, P. Caroff, H. Xu, *Nano Lett.* **2012**, *12*, 6414.
[6] R. M. Lutchyn, E. P. Bakkers, L. P. Kouwenhoven, P. Krogstrup, C. M. Marcus, Y. Oreg, *Nat. Rev. Mater.* **2018**, *3*, 52.
[7] S. Plugge, A. Rasmussen, R. Egger, K. Flensberg, *New J. Phys.* **2017**, *19*, 012001.
[8] D. J. Carrad, M. Bjergfelt, T. Kanne, M. Aagesen, F. Krizek, E. M. Fiordaliso, E. Johnson, J. Nygård, T. S. Jespersen, *Adv. Mater.* **2020**, *32*, 1908411.
[9] S. Heedt, M. Quintero-Pérez, F. Borsoi, A. Fursina, N. van Loo, G. P. Mazur, M. P. Nowak, M. Ammerlaan, K. Li, S. Korneychuk, J. Shen, M. A. Y. van de Poll, G. Badawy, S. Gazibegovic, N. de Jong, P. Aseev, K. van Hoogdalem, E. P. A. M. Bakkers, L. P. Kouwenhoven, *Nat. Commun.* **2021**, *12*, 4914.
[10] F. Borsoi, G. P. Mazur, N. van Loo, M. P. Nowak, L. Bourdet, K. Li, S. Korneychuk, A. Fursina, J.-Y. Wang, V. Levajac, E. Memisevic, G. Badawy, S. Gazibegovic, K. van Hoogdalem, E. P. A. M. Bakkers, L. P. Kouwenhoven, S. Heedt, M. Quintero-Pérez, *Adv. Func. Mater.* **2021**, *31*, 2102388.
[11] J. Shen, S. Heedt, F. Borsoi, B. Van Heck, S. Gazibegovic, R. L. O. het Veld, D. Car, J. A. Logan, M. Pendharkar, S. J. Ramakers, G. Wang, D. Xu, D. Bouman, A. Geresdi, C. J. Palmstrøm, E. P. A. M. Bakkers, L. P. Kouwenhoven, *Nat. Commun.* **2018**, *9*, 4801.
[12] A. E. Antipov, A. Bargerbos, G. W. Winkler, B. Bauer, E. Rossi, R. M. Lutchyn, *Phys. Rev. X* **2018**, *8*, 031041.
[13] M. W. A. de Moor, J. D. S. Bommer, D. Xu, G. W. Winkler, A. E. Antipov, A. Bargerbos, G. Wang, N. van Loo, R. L. M. O. het Veld, S. Gazibegovic, D. Car, J. A. Logan, M. Pendharkar, J. S. Lee, E. P. A. M. Bakkers, C. J. Palmstrøm, R. M. Lutchyn, L. P. Kouwenhoven, H. Zhang, *New J. Phys.* **2018**, *20*, 103049.
[14] S. Ahn, H. Pan, B. Woods, T. D. Stanescu, S. Das Sarma, *Phys. Rev. Mater.* **2021**, *5*, 124602.
[15] M. Pendharkar, B. Zhang, H. Wu, A. Zarassi, P. Zhang, C. P. Dempsey, J. S. Lee, S. D. Harrington, G. Badawy, S. Gazibegovic, R. L. M. Op het Veld, M. Rossi, J. Jung, A.-H. Chen, M. A. Verheijen, M. Hocevar, E. P. A. M. Bakkers, C. J. Palmstrøm, S. M. Frolov, *Science* **2021**, *372*, 508.
[16] J. Paajaste, M. Amado, S. Roddaro, F. Bergeret, D. Ercolani, L. Sorba, F. Giazotto, *Nano Lett.* **2015**, *15*, 1803.
[17] T. Kanne, M. Marnauza, D. Olsteins, D. J. Carrad, J. E. Sestoft, J. de Bruijckere, L. Zeng, E. Johnson, E. Olsson, K. Grove-Rasmussen, J. Nygård, *Nat. Nanotechnol.* **2021**, *16*, 776.
[18] M. S. Bjergfelt, D. J. Carrad, T. Kanne, E. Johnson, E. M. Fiordaliso, T. S. Jespersen, J. Nygård, *Nano Lett.* **2021**, *21*, 9875.
[19] J. M. Baker, C. J. Kircher, J. Matthews, *IBM J. Res. Dev.* **1980**, *24*, 223.
[20] S. A. Khan, C. Lampadaris, A. Cui, L. Stampfer, Y. Liu, S. J. Pauka, M. E. Cachaza, E. M. Fiordaliso, J.-H. Kang, S. Korneychuk, T. Mutas, J. E. Sestoft, F. Krizek, R. Tanta, M. C. Cassidy, T. S. Jespersen, P. Krogstrup, *ACS Nano* **2020**, *14*, 14605.
[21] B. S. Chandrasekhar, *Appl. Phys. Lett.* **1962**, *1*, 7.
[22] A. M. Clogston, *Phys. Rev. Lett.* **1962**, *9*, 266.
[23] P. M. Tedrow, R. Meservey, *Phys. Rev. B* **1982**, *25*, 171.
[24] See Supporting Information.
[25] P. Monceau, *Phys. Lett. A* **1974**, *47*, 193.
[26] X. S. Wu, P. W. Adams, Y. Yang, R. L. McCarley, *Phys. Rev. Lett.* **2006**, *96*, 127002.
[27] A. McAlister, D. Kahan, *Bull. Alloy Phase Diagrams* **1986**, *7*, 47.
[28] W. Wu, P. Adams, *Phys. Rev. Lett.* **1995**, *74*, 610.
[29] M. Tinkham, *Introduction to Superconductivity*, 2nd edition, Dover, Mineola, NY **2004**.
[30] L. D. Alegria, C. G. Bøttcher, A. K. Saydjari, A. T. Pierce, S. H. Lee, S. P. Harvey, U. Vool, A. Yacoby, *Nat. Nanotechnol.* **2021**, *16*, 404.
[31] R. Meservey, P. Tedrow, *Phys. Rep.* **1994**, *238*, 173.
[32] J. Alexander, T. Orlando, D. Rainer, P. Tedrow, *Phys. Rev. B* **1985**, *31*, 5811.
[33] S. M. Albrecht, A. P. Higginbotham, M. Madsen, F. Kuemmeth, T. S. Jespersen, J. Nygård, P. Krogstrup, C. Marcus, *Nature* **2016**, *531*, 206.
[34] A. Savin, M. Meschke, J. P. Pekola, Y. A. Pashkin, T. Li, H. Im, J.-S. Tsai, *Appl. Phys. Lett.* **2007**, *91*, 063512.
[35] J. Shen, G. W. Winkler, F. Borsoi, S. Heedt, V. Levajac, J.-Y. Wang, D. van Driel, D. Bouman, S. Gazibegovic, R. L. M. Op Het Veld, D. Car, J. A. Logan, M. Pendharkar, C. J. Palmstrøm, E. P. A. M. Bakkers, L. P. Kouwenhoven, B. van Heck, *Phys. Rev. B* **2021**, *104*, 045422.
[36] G. E. Blonder, M. Tinkham, T. M. Klapwijk, *Phys. Rev. B* **1982**, *25*, 4515.
[37] S. Das Sarma, J. D. Sau, T. D. Stanescu, *Phys. Rev. B* **2012**, *86*, 220506.
[38] E. Prada, P. San-Jose, M. W. de Moor, A. Geresdi, E. J. Lee, J. Klinovaja, D. Loss, J. Nygård, R. Aguado, L. P. Kouwenhoven, *Nat. Rev. Phys.* **2020**, *2*, 575.
[39] H. Pan, C.-X. Liu, M. Wimmer, S. Das Sarma, *Phys. Rev. B* **2021**, *103*, 214502.
[40] D. Puglia, E. A. Martinez, G. C. Ménard, A. Pöschl, S. Gronin, G. C. Gardner, R. Kallaher, M. J. Manfra, C. M. Marcus, A. P. Higginbotham, L. Casparis, *Phys. Rev. B* **2021**, *103*, 235201.
[41] T. O. Rosdahl, A. Vuik, M. Kjaergaard, A. R. Akhmerov, *Phys. Rev. B* **2018**, *97*, 045421.
[42] D. I. Pikulin, B. van Heck, T. Karzig, E. A. Martinez, B. Nijholt, T. Laeven, G. W. Winkler, J. D. Watson, S. Heedt, M. Temurhan, V. Svidenko, R. M. Lutchyn, M. Thomas, G. de Lange, L. Casparis, C. Nayak, *arXiv:2103.12217* **2021**.
[43] E. J. Lee, X. Jiang, M. Houzet, R. Aguado, C. M. Lieber, S. De Franceschi, *Nat. Nanotechnol.* **2014**, *9*, 79.
[44] A. Jellinggaard, K. Grove-Rasmussen, M. H. Madsen, J. Nygård, *Phys. Rev. B* **2016**, *94*, 064520.